ACS Catalysis

pubs.acs.org/acscatalysis

Research Article

Increasing the Oxygen-Evolution Reaction Performance of Nanotubular Titanium Oxynitride-Supported Ir Nanoparticles by a Strong Metal–Support Interaction

Marjan Bele, Primož Jovanovič,* Živa Marinko, Sandra Drev, Vid Simon Šelih, Janez Kovač, Miran Gaberščček,* Gorazd Koderman Podboršek, Goran Dražić, Nejc Hodnik, Anton Kokalj, and Luka Suhadolnik*

Cite This: *ACS Catal.* 2020, 10, 13688–13700

Read Online

ACCESS | Metrics & More | Article Recommendations | Supporting Information

ABSTRACT: This study targets one of the grand challenges of electrochemical hydrogen production: a durable and cost-effective oxygen-evolution catalyst. We present a thin-film composite electrode with a unique morphology and an ultralow loading of iridium that has extraordinary electrocatalytic properties. This is accomplished by the electrochemical growth of a defined, high-surface-area titanium oxide nanotubular film, followed by the nitridation and effective immobilization of iridium nanoparticles. The applicative relevance of this production process is justified by a high oxygen-evolution reaction (OER) activity and high stability. Enhanced OER performance is due to the strong metal–support interaction (SMSI). The high durability is achieved by self-passivation of the titanium oxynitride (TiON) surface layer with TiO_2, which in addition also effectively embeds the Ir nanoparticles while still keeping them electrically wired. An additional contribution to the enhanced durability comes from the nitrogen atoms, which according to our density functional theory (DFT) calculations reduce the tendency of the Ir nanoparticles to grow. Materials are analyzed by advanced electrochemical characterization techniques. Namely, the entire process of the TiON–Ir electrode's preparation and the electrochemical evaluation can be tracked with scanning electron microscopy, X-ray diffraction (XRD), and X-ray photoelectron spectroscopy (XPS) at identical locations. In general, the experimental approach allows for the unique morphological, structural, and compositional insights into the preparation and electrocatalytic performance of thin films, making it useful also outside electrocatalysis applications.

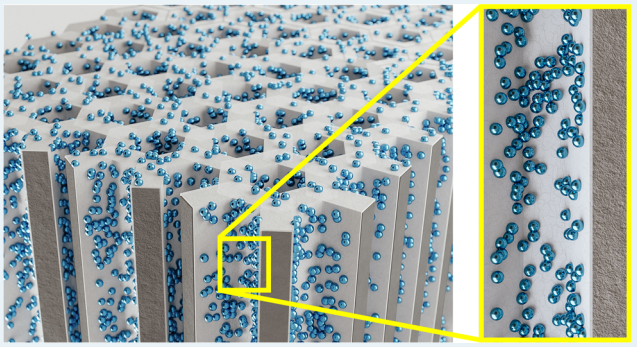

KEYWORDS: *electrocatalysis, oxygen-evolution reaction, TiON–Ir-nanotube catalyst, thin-film electrode, titanium oxynitride nanotubular support, TiON–Ir catalyst, iridium nanoparticles, IL-SEM*

1. INTRODUCTION

In the field of electrocatalysis, catalytic materials are utilized in the form of a high-surface-area, highly conductive thin film. The benefits of such materials are the good accessibility of the reactants and the assurance of good electrical contacts with the supporting material. However, the design of such materials is often challenging due to the harsh electrochemical environment that leads to degradation of the thin-film catalyst.[1] This is especially true for the oxygen-evolution reaction (OER), where electrochemical conditions are more severe in comparison to other reactions of the energy-conversion sector. Ruthenium and iridium oxides are the material of choice for OER.[2−6] Especially, iridium, due to its high price, must be dispersed on a substrate with a high surface area to increase the utilization of the catalyst layer.[7−10] Among OER thin-film approaches, the state of the art are still dimensionally stable anodes (DSAs) that are synthesized by the co-precipitation of RuO_2 and IrO_2 oxides supported by a titanium substrate with a thickness of a few micrometers.[11−15] This results in a high crystallinity as well as mechanical and electrochemical stability, both of which meet industrial demands for long-term operation. Although these electrodes are very stable, they require high noble-metal loadings. As iridium is one of the scarcest metals on earth as well as being geologically unevenly distributed (it is predominantly concentrated in the Republic of South Africa), it is of the highest importance to utilize it as effectively as possible if the technology of electrochemical hydrogen

Received: August 24, 2020
Revised: October 29, 2020
Published: November 10, 2020

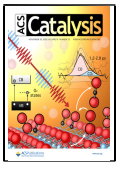

https://dx.doi.org/10.1021/acscatal.0c03688
ACS Catal. 2020, 10, 13688–13700

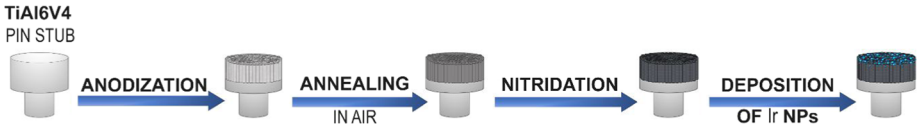

Figure 1. Procedure for preparing the immobilized TiON–Ir thin-film electrode.

production is to be scaled up. For example, one of the best polymer electrolyte membrane (PEM) electrolyzers in terms of iridium-anode loading (0.25 mg cm^{-2})[16] obtained so far still means that approximately 100 tons of iridium would be needed to produce devices that generate hydrogen at a rate equivalent to 1 TW of energy storage (1 TW_{H_2}). Considering that the current annual global production of iridium is merely <10 tons,[17] only a significant improvement in iridium utilization can justify the economic feasibility of PEM electrolyzers.

In this respect, dispersing the Ir catalysts on a high-surface-area support would provide the desired lowering of the noble-metal loading. However, as carbon-based supports, otherwise the most commonly used in electrocatalysis, are unstable under OER electrochemical conditions,[18−20] alternative solutions are needed.[21] In order for such composites to be industrially relevant, their preparation should be as scalable and straightforward as possible. In this respect, the electrolyzer technology would benefit even more if such a synthesis provided an immobilized catalyst that can be directly used as an electrode rather than a catalyst in the form of a powder.

Considering the above requirements, electrochemical anodization (oxidation) seems an appropriate platform.[22] Furthermore, this method enables the growth of oxide nanostructures of different morphologies.[23] The most well-known and studied are TiO_2 nanotubes,[24] which, however, cannot be used for electrochemical applications exhibiting high current densities, since titanium dioxide is a semiconductor and thus might not provide sufficient electrical conductivity.

There have been many attempts to increase the electrical conductivity of TiO_2 nanotubes.[25] One of the most important ways to change the properties of titanium dioxide is its conversion into other compounds that can have different properties, including electrical conductivity. Examples of these materials include barium titanate[26] and strontium titanate,[27] both of which retain their nanotubular structure after the transformation during a hydrothermal treatment. These materials are used primarily for sensor applications.[28] On the other hand, conductive titanium oxynitride (TiON) is also a very promising candidate for electrocatalytic applications;[29,30] however, it is rarely employed for the OER. Besides our recent studies,[17,31] there have been no other reports dealing with Ti oxynitrides in conjunction with Ir.

In this investigation, we focus on the development of a novel thin-film electrode material for the oxygen-evolution reaction that exhibits an extraordinarily high OER activity and good stability. The beneficial properties of our thin-film OER electrode are in our opinion due to the strong metal–support interaction or SMSI effect, which we support by experimental data and also the density-functional-theory (DFT) calculations. To obtain an in-depth insight into the development of the material's features during its synthesis, as well as the impact on the final properties, we used a unique characterization approach. Namely, for the first, the entire process of electrocatalyst preparation and electrochemical operation was tracked with the so-called identical-location scanning electron microscopy (IL-SEM), X-ray diffraction (XRD), and X-ray photoelectron spectroscopy (XPS) techniques.

2. EXPERIMENTAL SECTION

2.1. Synthesis of the TiON–Ir Catalyst. The TiON–Ir catalyst was prepared in an immobilized form following the procedure shown in Figure 1. In the first step, the TiAl6V4 (90 wt % Ti, 6 wt % Al, 4 wt % V) alloy in the shape of an scanning electron microscopy (SEM) pin stub was subjected to potentiostatic anodization in a two-electrode electrochemical cell using a stainless-steel counter electrode (Figure S1a). The titanium alloy was first cleaned with acetone and ethanol in an ultrasonic bath and then anodized in an electrolyte consisting of 0.3 wt % NH_4F (99.99%, Sigma-Aldrich) and 2 vol % deionized water in ethylene glycol (99.5%, Carlo Erba Reagents). The anodizing voltage was kept constant at 60 V, and the anodizing time was 30 min. The procedure resulted in an amorphous TiO_2 nanotube film, which was then washed with deionized water and ethanol and annealed at 450 °C for 1 h. After the conversion of the amorphous TiO_2 phase into the anatase phase, a second annealing was performed in an ammonia atmosphere at 700 °C for 10 h to convert the crystalline TiO_2 nanotube arrays into the TiON substrate. The flow of pure ammonia gas was kept constant at 50 cm^3 min^{-1} and a pressure of 1 atmosphere. In the last step, iridium nanoparticles were deposited on the TiON substrate. To deposit the iridium particles on the TiON substrate, the following procedure was developed. First, 15 mg of iridium-(III) bromide hydrate (Sigma-Aldrich, St. Louis, MO) was dissolved in 1.5 mL of water at 50 °C. Then, the solution was dip-coated on the TiON substrate with a withdrawal speed of 1 cm s^{-1} and dried at 50 °C. Afterwards, the sample was thermally treated in a 5% H_2/Ar mixture. The temperature was increased with a rate of 2 °C min^{-1} to 400 °C for 1 h, with the subsequent cooling rate to room temperature being 3 °C min^{-1}.

To compare the activity of the TiON–Ir catalyst with that of the TiO_2–Ir catalyst, another sample was prepared using the same procedure but without the nitridation step. The TiAl6V4 alloy was chosen as the starting material since it is the most commonly used titanium alloy known from a wide range of applications. To observe the morphological differences between the anodized TiAl6V4 alloy and the pure titanium, a grade-2 titanium foil was anodized under the same conditions.

2.2. Material Characterization. Each step of the synthesis process was studied with IL-SEM described in the Supporting Information (Section S2).[32−34] In this way, we were able to observe the same site on the sample throughout the entire synthesis process and after the electrochemical analysis. The evolution of the morphology was studied with a Zeiss FE-SEM SUPRA 35 VP field-emission scanning electron microscope (Carl Zeiss, Oberkochen, Germany). Detailed investigations of the TiO_2 and TiON structural and elemental features were performed using a conventional 200 kV transmission electron microscope (JEM-2010F, JEOL, Japan). Chemical analyses

https://dx.doi.org/10.1021/acscatal.0c03688
ACS Catal. 2020, 10, 13688−13700

were performed using a Si(Li) energy-dispersive spectroscopy (EDS) detector. Each step of the TiON−Ir preparation was also characterized by X-ray diffraction. The X-ray diffractograms of the samples were recorded on a flat, disclike Si sample holder with a PANalytical X'Pert PRO MPD X-ray powder diffractometer (PANalytical B.V., Almelo, The Netherlands) with a radiation wavelength Cu $K\alpha_1$ = 1.5406 Å in the α_1 configuration with a Johansson monochromator on the primary side. The diffractograms were recorded with a 0.034° resolution and 100 s signal-integration time in the 2θ range from 10 to 80° with a scanning X'Celerator detector (full open 2.122° 2θ). The 0.02 rad Soller slits and 10 mm divergent slits were used together with a 10 mm beam mask. The phases were identified using the X'Pert HighScore Plus program and the International Centre for Diffraction Data (ICDD) PDF-4+ 2016 database.[35] The surface of the TiON−Ir catalyst (the upper 3−5 nm) was also characterized using X-ray photoelectron spectroscopy (XPS) on a PHI-TFA XPS spectrometer produced by Physical Electronics Inc. and equipped with an Al-monochromatic source. The sample was analyzed before and after the electrochemical measurements to observe the changes to the structure and the composition during the degradation protocol. Brunauer−Emmett−Teller (BET) surface-area and nitrogen-sorption measurements of the TiO_2 and TiON supports in powder form were recorded using a Tristar 3000 automated gas-adsorption analyzer (Micromeritics Instrument Corp.) at 77 K. The BET surface area was calculated using the adsorption branch in the relative pressure range between 0.29 and 0 bar. The iridium content was determined according to the following protocol. The sample was submerged in 8 mL of hot aqua regia (80 °C, 3:1 HCl/HNO_3 v/v, concentrated) and intensely sonicated for 90 min. During this time, all of the dark surface coating, containing elemental Ir and the underlying substrate, was etched away and dissolved into the aqua regia. The latter was subsequently diluted with Milli-Q water to 50 mL, and the Ir concentration was measured with an inductively coupled plasma-optical emission spectrometry (ICP-OES) instrument (Varian 715-ES) by standard procedures (using external calibration by traceable Ir standard solution). The net mass of Ir on the sample was then calculated from the concentrations determined. In the case of the sample that was electrochemically analyzed, the mass of Ir was 0.85 μg, which resulted in an Ir loading of 1.7 $\mu g\ cm_{geom}^{-2}$. To confirm that the Ir was completely removed from the underlying substrate, we repeated the etching procedure. In this case, the Ir signal was below the limit of detection, proving full removal of the surface coating.

2.3. Electrochemical Measurements. *2.3.1. IL-SEM Electrodes.* Experiments were performed in a single-compartment three-electrode cell with a Ag/AgCl reference electrode and a graphite-rod counter electrode. The working electrode was positioned at the bottom of the cell with the catalyst surface facing upward. The electrochemical cell used for the determination of catalytic activity was the same as the one used for the anodic oxidation of the starting TiAl6V4 pin stub to ensure that there were no electrochemical contributions from the metal pin stub that held the electrocatalyst (Figure S1b). The working electrode consisted of a metallic holder with an SEM pin stub (the same as used in the synthesis of the catalytic composite). An aqueous solution of 0.1 M $HClO_4$ (Merck, Suprapur, 70%, diluted by Milli-Q, 18.2 MΩ cm) was used as the supporting electrolyte. IR resistance between the working and reference electrode was measured using the high-frequency intercept of an impedance scan (measured at open-circuit potential (OCP)). Ohmic drop compensation (85%) was applied during electrochemical experiments via positive feedback mode. All of the potentials of the reported electrochemical experiments refer to the reversible hydrogen electrode (RHE). The RHE potential was measured by saturating the electrolyte with hydrogen and measuring the open-circuit potential (OCP). Prior to the electrochemical characterization of the TiON−Ir, the catalyst was preactivated by a galvanostatic treatment (5 mA cm_{geom}^{-2} for 30 min). The activation step is necessary to diminish the Faradaic contribution of the TiON support under OER conditions (as shown in the continuation, the XPS analyses reveal that TiON undergoes a chemical modification due to electrochemical oxidation during the OER conditions). The OER activities of four Ir-based catalysts were evaluated using linear-sweep voltammetry (LSV) with a scan rate of 20 mV s^{-1} in the potential window between 0.3 and 1.8 V. The degradation protocol consisted of an LSV potential increase from 0.3 to 1.8 V and holding the potential at 1.8 V for 60 min. After the degradation protocol, LSV was performed under the same conditions as prior to the potentiostatic degradation. Such an electrochemical protocol was used to study the activity of all three prepared samples: two TiON-based Ir catalysts and a TiO_2-based Ir catalyst. In the case of the TiON−Ir samples, one sample was used to study the morphological changes during each synthesis step and to observe the morphological changes after the electrochemical treatment. Another sample was prepared to compare its electrochemical performance with the TiO_2−Ir analogue (results are shown in the Section S12, Supporting Information).

2.3.2. Electrochemical Treatment of IL-SEM Electrodes for XPS. XPS analyses were performed on a separate TiON−Ir sample, which was prepared in the same way as the primary TiON−Ir analogue. The XPS analyses were performed prior to and after the electrochemical protocol, which consisted of a 30 min potentiostatic (1.6 V vs RHE) treatment.

2.3.3. Rotating-Disc-Electrode (RDE) Measurements. The electrochemical performances were compared to a commercial Ir analogue, i.e., "Ir Black" (Alfa Aesar, 99.95% CAS: 7439-88-5). The electrochemical characterization of this sample was performed in a rotating-disc-electrode (RDE) configuration, as follows. A conventional three-electrode setup consisting of a gold disc electrode (d = 4 mm), a graphite rod as the counter electrode, and a Ag/AgCl reference electrode was used. The last of these was separated from the main cell compartment by a Luggin capillary. Deaerated 0.1 M $HClO_4$ (Merck, Suprapur, 70%, diluted by Milli-Q, 18.2 MΩ cm) was used as the working electrolyte. For the preparation of the electrode, a standard ink containing 1.4 mg of Ir was dispersed in 3 mL of water, 0.96 ml of 2-propanol, and 16 μL of Nafion (5 wt %, Sigma-Aldrich).[36] The ink was bath-sonicated for 20 min; following sonication, 10 μL aliquots were pipetted onto polished polycrystalline gold electrodes, resulting in a loading of 27.5 $\mu g_{Ir}\ cm_{geom}^{-2}$. Before any activity measurements, the sample was electrochemically oxidized with 200 potential cycles (300 mV s^{-1}) between 0.05 and 1.2 V vs RHE to provide for a stable cyclic voltammetry (CV). The electrolyte was changed before the activity measurement to avoid any trace of contamination. The OER activity was evaluated using the same protocol as in the case of the IL-SEM holder, i.e., LSV with a scan rate of 20 mV s^{-1} in a potential window

https://dx.doi.org/10.1021/acscatal.0c03688
ACS Catal. 2020, 10, 13688−13700

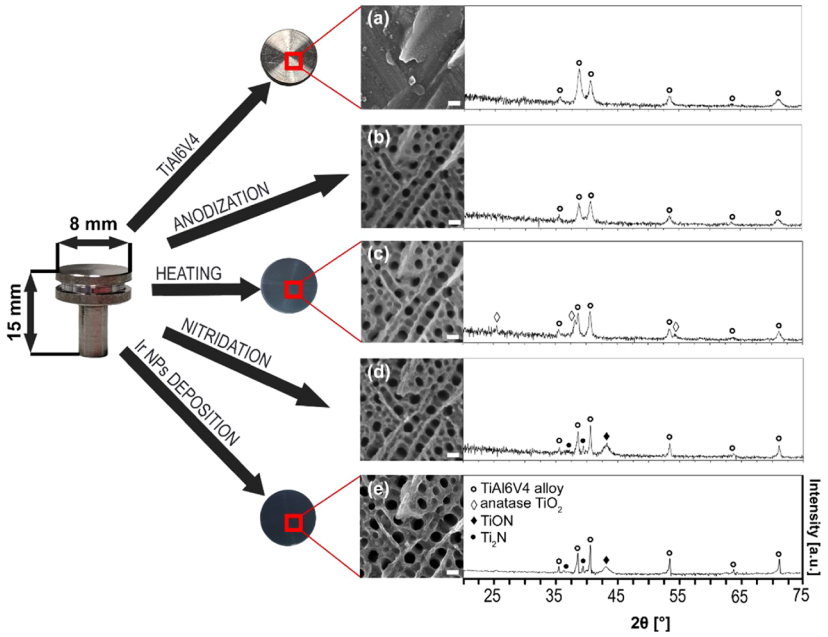

Figure 2. Top-view IL-SEM images (identical location) of our sample throughout the entire synthesis process and corresponding XRD analyses. (a) Starting TiAl6V4 alloy, (b) anodized starting material, (c) TiO_2 nanotubes annealed in air, (d) sample after annealing in ammonia, and (e) final TiON−Ir catalyst. Scale = 100 nm.

between 0.3 and 1.8 V. The degradation protocol consisted of an LSV potential increase from 0.3 to 1.8 V and holding the potential at 1.8 V for 30 min. After the degradation protocol, LSV was performed under the same conditions as prior to the potentiostatic degradation. Throughout the entire electrochemical treatment, a rate of 2500 rotations per minute (rpm) was used to lower the blocking effect of evolved oxygen bubbles.[37] We note that initially two different loadings were tested, 27.5 and 55 $\mu g_{Ir}\ cm_{geom}^{-2}$. The latter, however, resulted in severe blockage of oxygen bubbles. In the case of all of the electrochemical treatments, IR resistance between the working and reference electrode was measured using the high-frequency intercept of an impedance scan for each electrode (measured at open-circuit potential). Ohmic drop compensation (85%) was applied during electrochemical experiments via positive feedback mode.

2.4. DFT Calculations. DFT calculations were performed with the `PWscf` code from the `Quantum ESPRESSO` distribution[38] using the GGA + U method[39,40] with the exchange-correlation functional of Perdew−Burke−Ernzerhof (PBE).[41] Core electrons were described with the projector-augmented-wave (PAW) potentials, obtained from the pslibrary.[42,43] Kohn−Sham orbitals were expanded in a plane-wave basis set with a kinetic energy cutoff of 50 Ry (575 Ry for the charge density). A U parameter of 4.0 eV was used for the Ti ions. This U value was calculated self-consistently for the $Ti_{1.5}ON$ bulk using the hp.x code that utilizes a density-functional-perturbation-theory scheme.[44] The utilized model of $Ti_{1.5}ON$ bulk[a] can be described with a rock-salt crystal structure with two interpenetrating fcc latices of O/N anions and Ti cations (with 25% of vacancies); the two lattices are shifted by half a Bravais lattice vector with respect to one another. On average, there are seven atoms (three Ti, two N, two O) and one Ti vacancy in the unit cell (Figure S3a). Our calculated lattice parameter for the $Ti_{1.5}ON$ bulk is 4.172 Å, in good agreement with the experimental value.[a] Brillouin-zone integrations were performed with the uniformly shifted 4 × 4 × 4 k-mesh for the $Ti_{1.5}ON$ bulk (for the surface calculations, the k-grids were of comparable quality) and a Methfessel−Paxton smearing[45] of 0.02 Ry.

The high-angle annular dark-field scanning transmission electron microscopy (HAADF-STEM) experiments revealed that the dominant surface of the $Ti_{1.5}ON$ substrate is the (111). As a result, we described the $Ti_{1.5}ON$ substrate with the $Ti_{1.5}ON(111)$ slab. Its structure in the surface normal direction consists of Ti and O/N layers stacked one on top of the other. The $Ti_{1.5}ON(111)$ was modeled with a symmetric nonpolar slab consisting of five Ti layers terminated by O/N layers on both sides of the slab (Figure S3b): to maintain the stoichiometry, the surface O/N layers contain only 50% of the O and N ions. The largest considered surface model consists of a (3 × 3) supercell of $Ti_{1.5}ON(111)$ with the supercell vectors $|\boldsymbol{a}| = |\boldsymbol{b}| = 17.700$ Å, which was described by the γ k-point. All degrees of freedom were relaxed during the calculations.

The bonding of the Ir clusters to the $Ti_{1.5}ON(111)$ was analyzed by means of the electron-charge-density difference, $\Delta\rho(\boldsymbol{r})$, calculated as

$$\Delta\rho(\boldsymbol{r}) = \rho_{\mathrm{Ir}_n/\mathrm{TiON}}(\boldsymbol{r}) - \rho_{\mathrm{Ir}_n}(\boldsymbol{r}) - \rho_{\mathrm{TiON}}(\boldsymbol{r}) \quad (1)$$

where $\rho_{\mathrm{Ir}_n/\mathrm{TiON}}(\boldsymbol{r})$ is the electron charge density of the whole Ir_n cluster/$Ti_{1.5}ON(111)$ system, whereas $\rho_{\mathrm{Ir}_n}(\boldsymbol{r})$ and $\rho_{\mathrm{TiON}}(\boldsymbol{r})$ are the electron densities of the Ir_n cluster and the $Ti_{1.5}ON(111)$ slab, respectively, both having the same geometry as in the whole system.

The planar-integrated charge-density difference, $\Delta\rho(z)$, was calculated by integrating $\Delta\rho(\boldsymbol{r})$ by xy-slices spanned by the surface supercell, i.e.,

$$\Delta\rho(z) = \int_A \Delta\rho(x, y, z)\, \mathrm{d}x\, \mathrm{d}y \quad (2)$$

where A is the area spanned by the surface supercell and $\Delta\rho(x, y, z) \equiv \Delta\rho(\boldsymbol{r})$.

https://dx.doi.org/10.1021/acscatal.0c03688
ACS Catal. 2020, 10, 13688−13700

The adhesion energies of the Ir_n clusters on the $Ti_{1.5}ON$-(111) were calculated as

$$E_{adh} = E_{Ir_n/TiON} - E_{Ir_n} - E_{TiON} \quad (3)$$

where $E_{Ir_n/TiON}$, E_{Ir_n}, and E_{TiON} are the total (potential) energies of the relaxed Ir_n cluster/$Ti_{1.5}ON(111)$ system, the relaxed standalone Ir_n cluster, and the relaxed bare $Ti_{1.5}ON(111)$ slab, respectively.

For consistency reasons, with the designation used in the experimental counterpart of the article, the $Ti_{1.5}ON$ will be simply designated by the acronym TiON in the following.

3. RESULTS AND DISCUSSION

3.1. Characterization of the TiON−Ir Nanostructures.

Figure 2 shows the dimensions of the SEM pin stub together with the optical changes to its surface in three different phases of the TiON−Ir catalyst's preparation. The same figure also shows top-view SEM images of the same site of our sample throughout the entire synthesis process and the corresponding diffraction peaks from the XRD analyses. The surface color of the TiAl6V4 SEM pin stub is shown in Figure 2a. It was cleaned, but not polished, before use, which is why irregularities can be observed. After anodization, the surface changes to a high-surface-area, rigidly attached TiO_2 nanotubular film (Figure 2b), which retains its morphology after annealing at 450 °C (Figure 2c). A particularly important characteristic of the sample is that the surface of the film does not crack during the calcination, as this allows for controlled thin-film preparation. Macroscopic cracks, however, always occur during the calcination of the anodized (pure) titanium (Figure S6b). In the case of the anodized TiAl6V4 alloy, they do not appear due to better matching of the temperature expansion coefficients of the substrate and the nanostructured film (Figure S6a). Both films shown in Figure 3 were annealed at 450 °C for 1 h. Even in the next synthesis step, annealing in ammonia at 700 °C, cracks do not occur. The second annealing further increases the specific surface area, as determined with the BET analysis of the TiO_2 and TiON supports that were detached from the metal titanium substrate (29.1 ± 0.2 m^2 g^{-1} for TiO_2 in comparison to 36.3 ± 0.2 m^2 g^{-1} for TiON). It also establishes a good electronic conductivity of the supporting TiON material (Figure 2d).[46] In the last step, Ir nanoparticles were deposited; however, they are too small in terms of size and quantity to be visible in the SEM micrograph of Figure 2e. We note that at this point it is still unclear why favorably small Ir nanoparticles are formed on the TiON support. For example, the same procedure in the case of preparation of Pt nanoparticles resulted in much worse dispersion (not shown). An animation, showing the morphological changes throughout the synthesis process, is available online in the Supporting Information video clip.

The inner and outer diameters of the TiO_2 (Figure S7a) and TiON (Figure 3a) nanotubes estimated from the TEM top-sectional view of the nanotubes are approximately 70−80 and 100−120 nm in the case of the TiO_2 and 60−80 and 110−120 nm in the case of the TiON, respectively. The thickness of the TiO_2 nanotube wall is 30−40 nm (Figure S7b), and this decreases to 20 nm in the case of the TiON (Figure 3b). The reason for this significant morphological change is the change in the crystal structure that occurs during the insertion of N and the removal of O while TiO_2 transforms into TiON. The cross-sectional view of the TiO_2 and TiON nanotubes (Figures S7c and 3c) additionally shows diameters comparable with measurements in the top-sectional view. Moreover, the higher-magnification images of the top-sectional view of the TiO_2 (Figure S7d) and the TiON (Figure 3d) nanotubes reveal small polycrystalline grains with an approximate size of 15−20 nm. The length of the final catalyst in the form of the TiON−Ir nanotubes was determined on crushed particles of the nanotube films that were oriented perpendicular to the electron beam of SEM (not shown). The average measured length is between 1.2 and 1.4 μm. TEM was also used to determine the quantity and size of the Ir nanoparticles (Figure 3e,f). The average Ir particle size is 2.29 nm. Energy-dispersive X-ray spectroscopy (EDS) of parts with and without the Ir nanoparticles shows their distribution and quantity, which was determined to be 3 atom % (Figure 3f). This is also in line with the XPS analysis (Table 1).

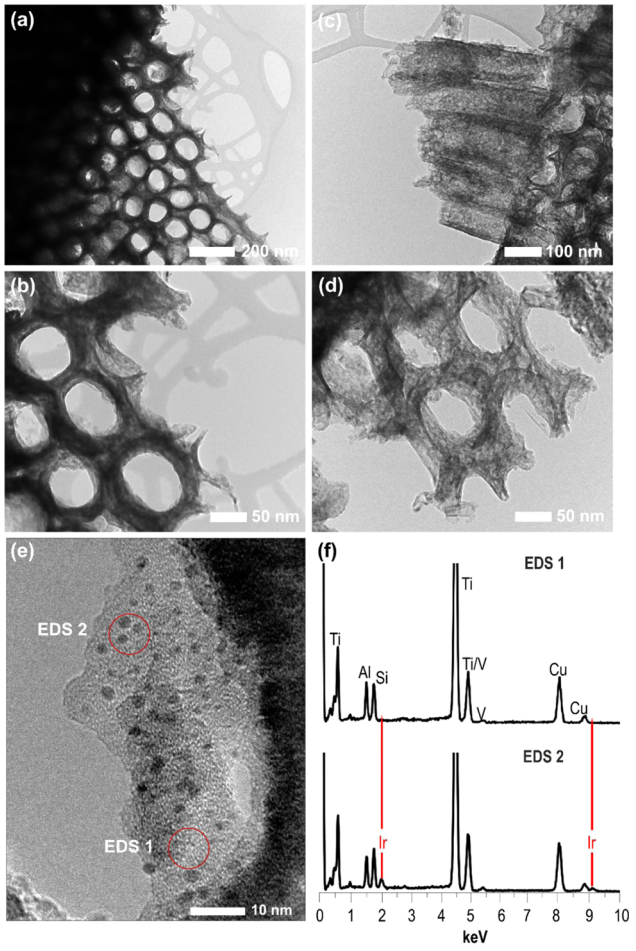

Figure 3. TEM micrographs of TiON nanotubes: (a) top-sectional view, (b) higher-magnification top-sectional view, (c) cross-sectional view, and (d) high-magnification top-sectional view. Figure (e) shows the TEM micrograph of the TiON nanotube with deposited Ir nanoparticles, whereas the corresponding EDS analyses of a part with no Ir nanoparticles (EDS 1) and a part with Ir nanoparticles (EDS 2) are shown in (f).

XRD analyses performed on the same SEM pin stub at all of the different synthesis stages for the catalyst preparation show the evolution of the crystallographic structure of the sample. All five diffractograms in Figure 2 show distinct peaks (○) related to the hexagonal aluminum titanium vanadium alloy at 2θ = 35.3° (100), 38.5° (002), 40.4° (101), 53.2° (102), and 70.9° (103) angles (PDF 04-002-8708).[35] The diffraction

https://dx.doi.org/10.1021/acscatal.0c03688
ACS Catal. 2020, 10, 13688−13700

Table 1. Surface Composition in atom % of the Sample before and after the Electrochemical Test Using the XPS Method

sample	N	O	Al	Ti	V	Ir
before the electrochemical test	19.8	49.5	5.2	19.7	1.9	3.8
after the electrochemical test	6.0	67.1	9.1	13.7	0.1	4.1

peaks corresponding to the titanium alloy support (Figure 2a) are observed in each synthesis step due to the small thickness of the nanotubular film. Anodization of the alloy results in uniform TiO_2 nanotube arrays with the presence of a small amount of vanadium and aluminum oxides, as shown by the EDS analyses in Figure 6 and by the XPS results (Table 1). We note that dissolution of vanadium and aluminum oxides under acidic conditions of a membrane electrode assembly (MEA) could cause potential issues in membrane conductivity;[47] hence, a V- and Al-free substrate or acid washing prior to implementation in a real device should be used. The TiO_2 nanotube film grown by anodic oxidation is amorphous, and only the diffraction peaks corresponding to the metal substrate can be observed (Figure 2b). Annealing at 450 °C for 1 h transforms the amorphous nanotubes into the anatase phase (Figure 2c). At the same time, it greatly improves the contact between the titanium alloy and the nanotubular film.[48] The additional diffraction peaks (◊) are related to the anatase phase of the tetragonal titanium oxide at 2θ = 25.4° (101), 38.1° (004), and 54.3° (105) angles (PDF 01-070-6826).[35] After the annealing in ammonia at 700 °C, the crystalline anatase TiO_2 is transformed into TiON (Figure 2d), which is firmly bound to the surface of the alloy due to the preliminary crystallization of the film at 450 °C. However, the surface of the titanium alloy lying beneath the TiON nanotubes is also nitrided to Ti_2N, as shown in Figure 2d. These additional diffraction peaks are related to (●) tetragonal titanium nitride at 2θ = 36.3° (200) and 39.3° (111) angles (PDF 04-001-9127)[35] and (♦) cubic titanium oxide nitride at 43.1° (200) angle (PDF 01-084-4872).[35] The XRD spectrum of the sample with Ir nanoparticles is shown in Figure 2e. There is no diffraction peak of the Ir due to the small size and quantity of the Ir nanoparticles. However, their presence was confirmed with EDS, the electrochemical analyses, TEM, and XPS (Figure 4b). The latter was used to determine the surface concentrations of the titanium, aluminum, vanadium, oxygen, nitrogen, and iridium and their oxidation states before and after the electrochemical measurements. The XPS spectra of Ir 4f and Ti 2p from the as-prepared sample are shown in Figure 4. It is clear that the Ir is mainly present in the metal state (80%), as evidenced by the Ir 4f peak at 60.8 eV, and partially in the Ir(4+) state (peak at 62.0 eV) in the as-prepared sample.[49] On this sample, the titanium is present in the Ti^{4+} (46%, peak at 458.3 eV), Ti^{3+} (23%, peak at 457.0 eV), and Ti^{2+} (31%, peak at 455.6 eV) oxidation states related to the TiO_2, Ti−O−N, and TiN species, respectively.[50] The nitrogen N 1s spectrum reveals its presence as nitride and oxynitride, having peaks at 396.5 and 398.0 eV. Aluminum and vanadium are in the form of oxides.

3.2. Electrochemical Performance: Initial OER Activity. In this work, the OER polarization curves are normalized per unit mass of iridium. The geometrical area of the normalized polarization curves can be manipulated by changing the loading of Ir. Hence, normalization by the geometrical area would not provide for a sufficient description of the electrochemical performance, especially if several electrocatalysts are compared. To compare different catalysts as intrinsically as possible, electrochemically active surface area (ECSA) should be determined. Only then, intrinsic (specific) activities could be obtained. However, there are several issues related to determining ECSA of the supported Ir-based electrocatalyst; hence, a rapid and accurate evaluation of the ECSA remains a challenging task. Unfortunately, in the case of Ir oxides, the active surface area cannot undergo proton underpotential deposition like platinum and other transition-metal electrocatalysts, making it difficult to estimate the ECSA, as well as the OER specific activity. Attempts have most definitely been made toward ECSA determination. One option is the employment of metal underpotential deposition (MUPD) such as mercury.[36,51,52] These methods, however,

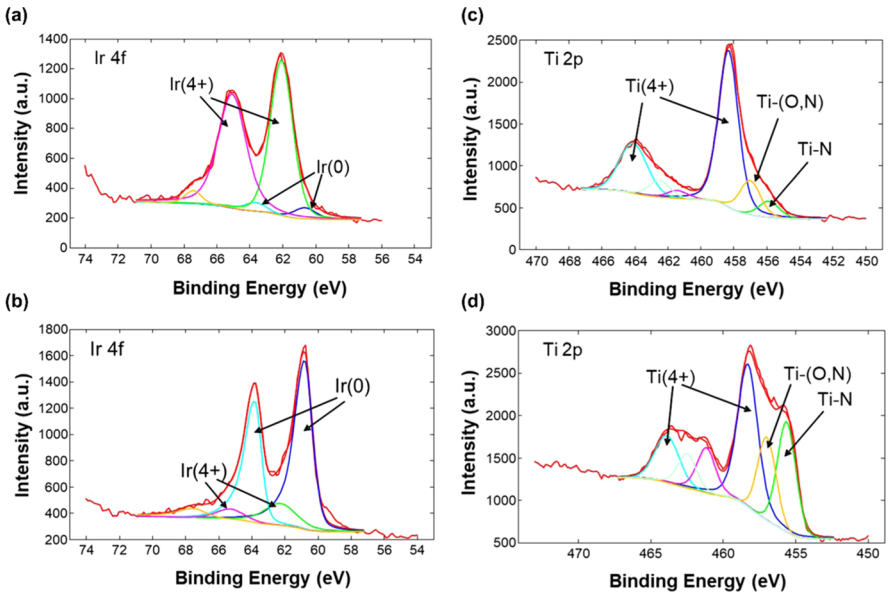

Figure 4. XPS spectra of Ir 4f and Ti 2p acquired on the sample before (b, d) and after the electrochemical test (a, c).

https://dx.doi.org/10.1021/acscatal.0c03688
ACS Catal. 2020, 10, 13688−13700

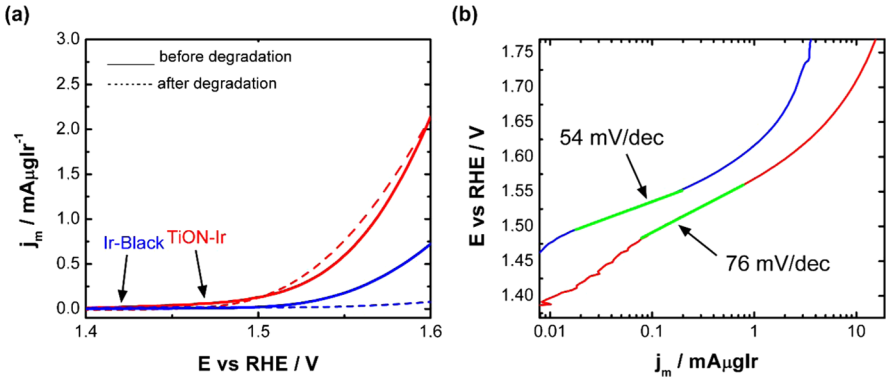

Figure 5. OER polarization curves of TiON−Ir (red line) and Ir Black (blue line) analogues before (solid line) and after (dashed line) the degradation protocol. (a) LSV response (20 mV s^{-1}) and (b) Tafel analysis.

suffer from possible cell contamination issues. The study of Savinell et al. demonstrates the usage of zinc ion adsorption to determine the ECSA of RuO_2 and IrO_2 analogues supported on a titanium substrate.[53] Briefly, their approach is based on establishing an empirical correlation between voltammetric charge and the ECSA, as measured by conventional surface area measurement techniques. The authors showed that ECSA is a linear function of voltammetric charge for RuO_2 and IrO_2 analogues. At this point, we want to note that oxide analogues enable obtaining reproducible voltammetric charge; hence, it is possible to develop an empirical correlation between voltammetric charge and the ECSA measured by conventional surface area measurement techniques. In our study, also nonoxide materials are investigated; hence, it is not possible to obtain a proper experimental correlation (such as presented by Savinell[53]). Another report dealing with ECSA for OER electrocatalysts, is given by Zhao et al.[54] Here, the authors propose a method to calculate the ECSA of iridium oxide in an operating PEM electrolyzer. A universal constant was obtained from the correlation of pseudocapacitive charge and ECSA of iridium oxide. In their work,[54] the Savinell method was improved by introducing a more accurate zinc concentration detection technique, UV−vis spectrophotometry. The methodology was applied to two distinct electrocatalyst systems (an electrochemically deposited IrO_x thin film and an IrO_x powder film), showing that the method gives microstructurally independent results. However, in their study,[54] a nonsupported Ir material was used, which would hinder the usage of the same methodology for the purpose of our study. Recently, McCrory et al.[55] demonstrated an approach to evaluate ECSA using electrochemical impedance spectroscopy (EIS). The concept is based on double-layer capacitance that is proportional to ECSA. However, this approach is not useful for characterizing supported materials as it does not consider double-layer contributions of the support. We note that in our case a supported Ir composite is investigated. Very recently, Bizzotto et al.[56] demonstrated that CO stripping could be used to determine the real surface area of Ir nanoparticles. However, the effectiveness of this concept can only be achieved if Ir surface is completely reduced; in the case of IrO_x CO, electrooxidation is inhibited. Therefore, authors have used CO stripping prior to OER characterization. Due to extremely small particle size, a significant portion of the Ir atoms are surface atoms (mean particle size of around 1.6 nm);[56] hence, surface roughening was considered negligible. We note, however, that in our case the particle size is larger; hence, surface roughening leading to alterations of a real surface can be expected during the OER. Only recently, Watzele et al. demonstrated an estimation of the real electroactive surface area of supported, nanostructured, oxide electrocatalysts using impedance measurements.[57] This concept is based on acquiring the values of the adsorption capacitance. We note that in our case the loading of Ir on high-surface-area TiON is extremely low (1.7 μg_{Ir} cm_{geom}^{-2}); hence, the relative portion of the TiON surface area is large. This makes obtaining a reliable value of the adsorption capacitance for the TiON−Ir composite highly challenging. Therefore, a proper methodology for the composites with ultralow Ir loading is yet to be developed and is a matter of ongoing investigation. This is one of the reasons that in this study we present the data as "current per mass of iridium". The other reason for such a presentation is that the mass activities are the most relevant parameter for real-application purposes. Nevertheless, a rough ECSA estimation was provided with the TEM analysis (∼100 m^2 g_{Ir}^{-1}; for details of determination, see the Section S6, Supporting Information) as well as via cyclovoltammetry (∼128 m^2 g_{Ir}^{-1}; for details of determination, see the Section S7, Supporting Information). Such values are relatively similar to the ECSA of supported Ir nanoparticles.[36,57] To place the catalytic performance of the TiON−Ir composite in the context of state-of-the-art OER electrocatalysts, its performance was compared to a commercial, nonsupported, Ir analogue (Ir Black) with the ECSA ranging between ∼23 and 30 m^2 g_{Ir}^{-1} (see the Section S9, Supporting Information).[36,51] The OER performance of the Ir Black analogue was evaluated under a rotating-disc-electrode (RDE) configuration (for details, see the Section 2). We note that caution should be taken when stationary (TiON−Ir) and rotating (Ir Black) OER electrodes are compared due to the gas-bubble effect. The latter is blocking the active sites. Hence, detachment of gas bubbles is essential for reaction proceeding at high potentials, and in this case, stationary and rotating electrodes cannot be adequately compared. However, if the absence of rotation (TiON−Ir case) would cause a significant effect, one would expect lower performance after the degradation protocol in comparison to Ir Black, which is not the case here (see Section 3.4).

The OER performances are compared in the kinetic region (up to 1.6 V, Figure 5a) because at higher potentials the OER polarization curve is not solely governed by its kinetics, but transport and the removal of the oxygen bubbles from the surface influence the current response.[37] The comparison

https://dx.doi.org/10.1021/acscatal.0c03688
ACS Catal. 2020, 10, 13688−13700

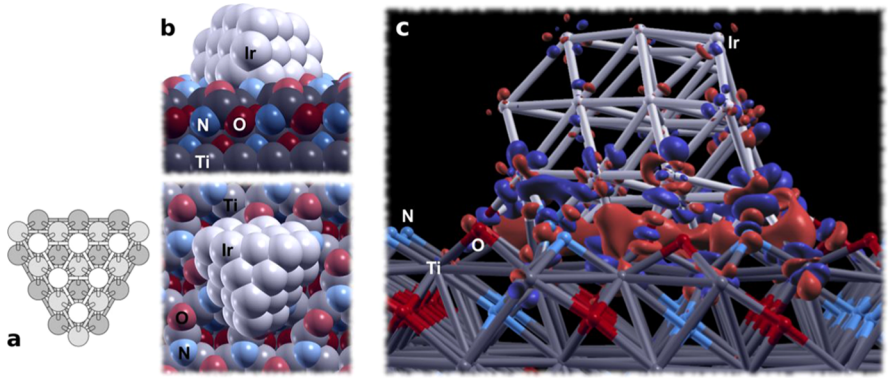

Figure 6. (a) Ideal structure of the $Ir_{[12,10,6]}(111)$ cluster and (b) its optimized structure on TiON. (c) Three-dimensional (3D) electron-charge-density difference, $\Delta\rho(r)$, of $Ir_{[12,10,6]}(111)$/TiON, calculated with eq 1. Isosurfaces of ±0.01 e b^{-3} are plotted. The red and blue colors represent the electron-excess and electron-deficit regions, respectively. Note the large electron-charge accumulation at the top O/N layer (red isosurfaces) and electron depletion of the bottom Ir layer (blue isosurfaces).

reveals that the TiON−Ir analogue significantly outperforms the Ir Black catalyst (Figure 5a solid line).

To explain the observed activity trends, several characteristics should be considered. First, the utilization of the iridium's ECSA is considerably better in the case of TiON−Ir (this is in line with approximately 4- 5-fold-larger ECSA, see above), which results in a higher mass activity. Second, in comparison to TiON−Ir, the Ir Black analogue has a lower electron mobility, since the electrode is prepared from a film of nanoparticles and does not allow one-dimensional charge transport, as in the case of vertically oriented nanotube-based films.[58] A similar effect has also been noticed in the case of TiON−Ir powder in our previous study.[59] It is important to stress that the average particle size of both analogues is very similar, i.e., 2.29 nm for TiON−Ir and 2.31 nm for Ir Black (see the Sections S6 and S8, Supporting Information). Hence, any particle-size-dependent activity effects should be ruled out when comparing the activities of both analogues. Last but not least, the existence of a strong interaction (commonly known as a strong metal−support interaction, SMSI) between the Ir and the TiON support should be taken into consideration. The benefits of SMSI in terms of catalytic activity were shown previously for other systems[60−62] and are now being progressively recognized also in the particular case of OER kinetics.[9,63] However, at this point, no direct evidence for SMSI between Ir and TiON is at hand. To further elucidate the activity difference, a Tafel slope analysis was performed (Figure 5b). Interestingly, the Tafel slope for TiON−Ir (76 mV dec^{-1}) is somewhat higher than expected (~40−50 mV dec^{-1} is common for Ir oxides[36]). By comparison, in the case of the Ir Black analogue, a slope of 54 mV dec^{-1} was obtained (Figure 5b). As mentioned, this difference cannot be due to the particle size, as it is almost identical for both samples. The same is true for other influential surface-related parameters such as facets, kinks, edges, and steps. Based on the present DFT calculations (see Section 3.3) and also referring to the literature data on similar systems,[9,62,63] it is reasonable to suggest that the OER mechanism, and thus the Tafel slope, is changed due to the interaction between the Ir nanoparticles and the support. It has been shown previously that an unusually large Tafel slope can be associated with such interactions when using semiconducting catalytic materials such as TiO_2 (see also Table S1),[64] so the steep Tafel slope could potentially be ascribed to this phenomenon. We ascribe more steep slope to an electrochemically formed TiO_2.[64] We confirm its presence by postmortem XPS analysis, which confirms that after the electrochemical test, the surface composition and structure of the same sample are changed significantly (Table 1). The surface of the TiON substrate is oxidized to a TiO_2-like structure (76%), but some of the Ti−N−O (16%) and TiN (8%) species are still present. The amount of oxygen is increased and the nitrogen is decreased. This finding is important since it proves that the surface TiON predominantly evolves to TiO_2 during the electrochemical operation. On the other hand, the concentration of Ir nanoparticles remains constant, although the Ir's oxidation state is changed to 4+, as evidenced by the peak at 62.0 eV (see Table 1). Unfortunately, from the XPS spectrum of the Ir 4f, it was not possible to distinguish between the possible presence of the Ir^{3+} and Ir^{4+} oxidation states due to the overlapping of these two components; hence, we cannot exclude the partial presence of Ir^{3+} in the sample after the electrochemical test. To elucidate the potential presence of interactions between the TiON support and Ir nanoparticles, DFT calculations were performed.

3.3. DFT Calculations of the Adhesion of the Ir Nanoparticles on the TiON Surface. To this end, Ir nanoparticles were modeled by small Ir_n clusters (n = 1, 4, 6, 7, 12, 13, 16, 19, and 28) consisting of one to three (111) layers. In addition, we also utilized models of two-layer rods, periodic in one direction, and commensurate overlayers. Snapshots of all of these models are shown in Figure S4. Single, standalone Ir atoms adhere most strongly to the TiON surface, with a magnitude of about 5 eV, while for larger clusters, the magnitude of the adhesion energy decreases as the cluster size increases and reaches about 1 eV/interface-Ir-atom for large clusters (Figure S5a). This reduction is a simple consequence of the fact that the stability of the clusters increases with the cluster size (Figure S5b). A standalone Ir atom can either adsorb into a vacancy of the TiON (note that the crystal structure of TiON contains 25% of Ti vacancies) or above the surface, such that it bonds simultaneously with one O and one N ion (the two possibilities are very similar in energy, within 0.1 eV). As for larger Ir ad-clusters, viable adhesion structures are commensurate with the fcc stacking of the TiON support.

To illustrate the adhesion bonding of the Ir nanoparticles to the TiON, the $Ir_{[12,10,6]}(111)$ ad-cluster is analyzed in Figure 6; $Ir_{[12,10,6]}(111)$ stands for a three-layer cluster consisting of

https://dx.doi.org/10.1021/acscatal.0c03688
ACS Catal. 2020, 10, 13688−13700

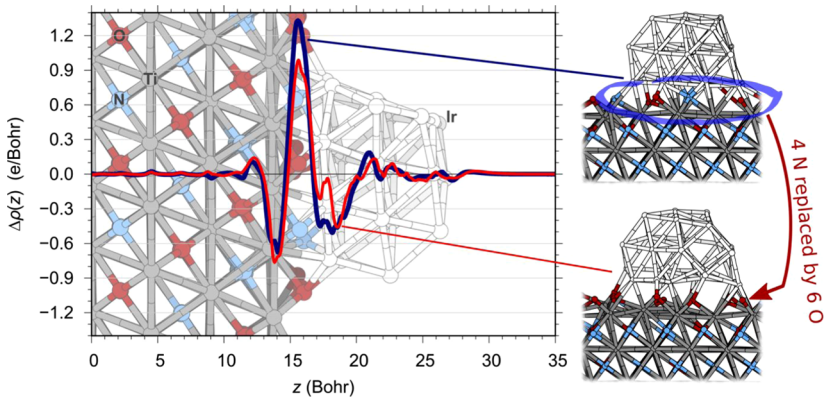

Figure 7. Planar-integrated electron-charge-density difference, $\Delta\rho(z)$, for $Ir_{[12,10,6]}(111)$ on TiON (blue curve), calculated with eq 2; $\Delta\rho(z) > 0$ means electron accumulation. The respective structure is superposed with the $\Delta\rho(z)$ curve to facilitate interpretation; $z = 0$ is arbitrarily set at the fourth Ti layer below the surface. Note that the top Ti layer (dark gray balls) and bottom Ir layer (white balls) loose electron charge ($\Delta\rho(z) < 0$), whereas the top O/N layer (red/blue balls) gains electron charge ($\Delta\rho(z) > 0$). The red curve represents the case where the N ions below the Ir cluster were replaced by O ions in a stoichiometric 2:3 ratio (i.e., four N were replaced with six O, as indicated by the sideview snapshots on the right). Note that the charge transfer is smaller in this case. In particular, the bottom Ir layer donates fewer electrons to the top O/N layer.

(111) layers with 12, 10, and 6 atoms in the bottom, middle, and top layers, respectively (Figure 6a). The optimized structure of the $Ir_{[12,10,6]}(111)$ on the TiON is shown in Figure 6b, while the adhesion bonding is illustrated in Figure 6c by means of the 3D electron-charge-density difference, $\Delta\rho(r)$ of eq 1. Note the large charge accumulation (red isosurfaces) around the N and O ions below the Ir ad-cluster. A charge depletion of the bottom Ir layer is also evidenced by the blue isosurfaces.

To further analyze the electron-charge transfer due to adhesion of the Ir ad-cluster on TiON, Figure 7 shows the planar-integrated electron-charge-density difference along the surface normal direction, $\Delta\rho(z)$ of eq 2, superposed with the respective structure so as to facilitate interpretation (blue curve). It is evident that the top Ti layer and the bottom Ir layer loose electron charge ($\Delta\rho(z) < 0$), whereas the top O/N layer (red/blue balls) in between the top Ti and the bottom Ir layers gains electron charge ($\Delta\rho(z) > 0$). The second Ir layer also gains a little electron charge, whereas the third (top) Ir layer is only marginally affected. This is a general pattern of electron-charge redistribution, also observed for other considered ad-clusters not shown here. So as to illuminate the role of the surface N ions in the adhesion of the Ir nanoparticles on the TiON, the red curve in Figure 7 represents the case where the N ions below the $Ir_{[12,10,6]}$ ad-cluster were replaced by O ions in a stoichiometric 2:3 ratio, i.e., four N were replaced with six O and the structure was relaxed. Note that the charge transfer is smaller in this case. In particular, the bottom Ir layer donates fewer electrons to the top O/N layer. The integration of $\Delta\rho(z)$ in the respective regions reveals that for the blue curve the bottom Ir and top Ti layers lose 1.15 and 0.75 electrons, respectively, whereas the top O/N layer gains 1.7 electrons and the middle Ir layer gains 0.2 electrons. For the red curve, which represents the case where N ions below the Ir cluster are replaced by O ions, the charge transfer is smaller: the top O/N gains 1.25 electrons and the bottom Ir layer loses 0.65 electrons (the respective numbers for the blue curve are 1.7 and 1.15). This clearly suggests that the N ions at the surface are better docking sites for the Ir nanoparticles than the O ions. This inference is corroborated by the observation that N ions also enhance the adhesion strength of the Ir clusters to the surface, compared to the O ions. In particular, the adhesion energy of the $Ir_{[12,10,6]}(111)$ cluster to TiON is −13.6 eV (per cluster), whereas if the four N ions below the Ir cluster are replaced by the six O ions, then the adhesion energy is considerably weaker, i.e., −7.9 eV. A similar N vs O trend in the charge transfer and the adhesion energy is also observed for the smaller $Ir_{[7,6,3]}(111)$ cluster (not shown).

The bottom line of these arguments is that the adhesion of Ir nanoparticles is enhanced by the N ions. Furthermore, it is usually assumed that the diffusion energy of the nanoparticles on the surface scales with the adhesion energy, i.e., the stronger is the adhesion, the larger is the diffusion barrier. This implies that the presence of N ions reduces the tendency of the Ir nanoparticles to sinter. Having small nanoparticles appears to be important, not only because in this way the fraction of surface Ir atoms is larger but because the analysis presented above reveals that the TiON substrate affects predominantly the electronic structure of the bottommost Ir layer, the layer above it is affected to a much smaller extent, whereas the modification of the third layer is already vanishing. Note that for more than two layers thick nanoparticles, only the "perimeter" sites of the two bottommost layers are exposed to the exterior environment. Provided that these perimeter sites are catalytically superior, this suggests that the nanoparticles should be small or the fraction of such perimeter sites is negligible. DFT stability prognosis was experimentally inspected by performing the electrochemical stability test.

3.4. Electrochemical Performance: Stability. To induce electrode degradation, a potentiostatic treatment at 1.8 V vs RHE was employed (we remark again that a degradation time of 1 h for the TiON−Ir and 30 min for the Ir Black was used). Note that this potential is significantly higher than normally used when simulating the practical working conditions of the catalyst layer. Here, we used high potentials to evaluate the durability in a relatively rapid manner. Obviously, the TiON−Ir analogue significantly outperforms the Ir Black catalyst (Figure 5a, dashed lines). This is in good agreement with the present DFT calculations, which reveal that the adhesion of Ir nanoparticle is enhanced by the presence of N ions (see Section 3.3). The stronger the adhesion, the larger is the diffusion barrier and thus the better the general performance of the material as particle coalescence is diminished. In fact,

https://dx.doi.org/10.1021/acscatal.0c03688
ACS Catal. 2020, 10, 13688−13700

rather surprisingly, in the case of TiON−Ir, the OER activity even slightly increased after the potentiostatic degradation, when compared to the initial activity. We note that more dedicated studies are needed to elucidate this unexpected effect, especially in the direction of monitoring electrochemically dissolved metal counterparts since at least some performance loss on the expense of dissolution would be expected at potentials of such magnitude (1.8 V vs RHE). These typically trigger the formation of soluble, higher-valent Ir oxide[65−67] as well as evolution of oxygen bubbles. The latter block the active surface area.[37] Effective detachment of gas bubbles is essential for efficient reaction proceeding at high potentials and decisively depends on electrode morphology.[37,68−73] For this purpose, morphological changes were inspected with the IL-SEM imaging. Fascinatingly, no significant changes to the TiON support morphology during the degradation protocol were observed (Figure S14), indicating promising characteristics of nanotubular morphology.

To the best of our knowledge, the present mass activity of TiON−Ir is the highest reported so far for OER catalysts consisting of pure Ir on a support (see Table S1). In fact, the only Ir-based catalysts with higher activity are the recently reported bimetallic Ir−Ni and Ir−Co nanowires[74,75] and Ir networks,[76] all of which belong to more complex materials, so a direct comparison is not possible. It is also important to note that in the present investigation a much more aggressive electrochemical treatment (1.8 V vs RHE) was used for the stability testing in comparison to the above-mentioned reports. Finally, we should note that in the case of the TiON−Ir the Ir geometric loading is approximately 150-fold smaller than in PEM electrolyzers with the best state-of-the-art performance.[16] We note that loadings of such low range are not expected to be incorporated in the real OER anode just yet, but the TiON−Ir composite could pave the way for lowering Ir content.[77]

5. CONCLUSIONS

This present investigation introduces a novel approach to the preparation and characterization of thin-film electrode composites. As a case example, a novel oxygen-evolution composite consisting of a thin-film electrode based on iridium nanoparticles dispersed on a nanotubular, high-surface-area, oxynitride support (TiON−Ir) is presented. The approach made possible an elegant characterization using the identical-location scanning electron microscopy (IL-SEM) and X-ray diffraction (XRD) techniques. In this way, the morphological and compositional changes to the TiON−Ir were successfully tracked through the whole synthesis and electrocatalytic processes. The mass activity of the present TiON−Ir material for the OER is one of the best measured so far for this reaction. Furthermore, employing a rigorous degradation protocol, a remarkable retention of electrochemical performance of the TiON−Ir composite was demonstrated as well. Importantly, the TiON support itself did not suffer any morphological changes during the electrochemical treatment. Based on complementary DFT modeling, the enhanced electrochemical performance is ascribed to a strong metal−support interaction (SMSI) between the Ir and the TiON. The presence of protective oxides, which hinders excessive oxidation of Ir, is an additional factor that can explain the excellent performance.

■ ASSOCIATED CONTENT

Supporting Information

The Supporting Information is available free of charge at https://pubs.acs.org/doi/10.1021/acscatal.0c03688.

Morphological changes throughout the synthesis process (MP4)

Setup for anodic oxidation and electrochemical characterization, description of IL-SEM, comparison of the electrochemical activity of the TiON−Ir and TiO_2−Ir, SEM of the TiON−Ir catalyst before and after the electrocatalytic measurements, additional TEM analysis, particle size determination and determination of ECSA, additional results of DFT calculations, and comparison of characteristic OER parameters with the state of the art (PDF)

■ AUTHOR INFORMATION

Corresponding Authors

Primož Jovanovič − *Department of Materials Chemistry, National Institute of Chemistry, SI-1000 Ljubljana, Slovenia;* orcid.org/0000-0003-2477-3895; Email: primoz.jovanovic@ki.si

Miran Gaberščček − *Department of Materials Chemistry, National Institute of Chemistry, SI-1000 Ljubljana, Slovenia;* orcid.org/0000-0002-8104-1693; Email: miran.gaberscek@ki.si

Luka Suhadolnik − *Department for Nanostructured Materials, Jožef Stefan Institute, SI-1000 Ljubljana, Slovenia;* orcid.org/0000-0002-9103-6687; Email: luka.suhadolnik@ijs.si

Authors

Marjan Bele − *Department of Materials Chemistry, National Institute of Chemistry, SI-1000 Ljubljana, Slovenia*

Živa Marinko − *Department for Nanostructured Materials, Jožef Stefan Institute, SI-1000 Ljubljana, Slovenia; Jožef Stefan International Postgraduate School, SI-1000 Ljubljana, Slovenia;* orcid.org/0000-0002-6054-8137

Sandra Drev − *Center for Electron Microscopy and Microanalysis, Jožef Stefan Institute, SI-1000 Ljubljana, Slovenia*

Vid Simon Šelih − *Department of Analytical Chemistry, National Institute of Chemistry, SI-1000 Ljubljana, Slovenia;* orcid.org/0000-0002-2433-5249

Janez Kovač − *Department of Surface Engineering and Optoelectronics, Jožef Stefan Institute, SI-1000 Ljubljana, Slovenia*

Gorazd Koderman Podboršek − *Department of Materials Chemistry, National Institute of Chemistry, SI-1000 Ljubljana, Slovenia; Jožef Stefan International Postgraduate School, SI-1000 Ljubljana, Slovenia*

Goran Dražić − *Department of Materials Chemistry, National Institute of Chemistry, SI-1000 Ljubljana, Slovenia*

Nejc Hodnik − *Department of Materials Chemistry, National Institute of Chemistry, SI-1000 Ljubljana, Slovenia; Jožef Stefan International Postgraduate School, SI-1000 Ljubljana, Slovenia;* orcid.org/0000-0002-7113-9769

Anton Kokalj − *Department of Physical and Organic Chemistry, Jožef Stefan Institute, SI-1000 Ljubljana, Slovenia; Jožef Stefan International Postgraduate School, SI-1000 Ljubljana, Slovenia;* orcid.org/0000-0001-7237-0041

Complete contact information is available at:
https://pubs.acs.org/10.1021/acscatal.0c03688

Notes

The authors declare no competing financial interest.

■ ACKNOWLEDGMENTS

The provision of financial support for the research and the preparation of the manuscript by the Slovenian Research Agency (ARRS) within the research programs P2-0084, P2-0152, and P2-0393 and projects Z2-8161, N2-0106, and Z1-9165 is gratefully acknowledged. The authors also thank Edi Kranjc (Department of Inorganic Chemistry and Technology, National Institute of Chemistry, Slovenia) for the X-ray powder-diffraction measurements.

■ ADDITIONAL NOTE

[a]The structural model for the $Ti_{1.5}ON$ bulk was constructed based on data for $Ti_{0.7}(N_{0.33}O_{0.67})$ (ICSD 426340),[75] with $Fm\bar{3}m$ structure and unit cell with a = 4.199 Å. From the electron energy loss spectroscopy (EELS) spectra of the investigated samples we measured that the concentrations of oxygen and nitrogen are approximately equal and therefore a small deviation from the original unit cell parameters was expected. Throughout the text we used the term TiON for the approximate formula Ti1.5ON.

■ REFERENCES

(1) Meier, J. C.; Galeano, C.; Katsounaros, I.; Witte, J.; Bongard, H. J.; Topalov, A. A.; Baldizzone, C.; Mezzavilla, S.; Schüth, F.; Mayrhofer, K. J. J. Design Criteria for Stable Pt/C Fuel Cell Catalysts. *Beilstein J. Nanotechnol.* **2014**, *5*, 44−67.
(2) Trasatti, S. Electrocatalysis by Oxides — Attempt at a Unifying Approach. *J. Electroanal. Chem. Interfacial Electrochem.* **1980**, *111*, 125−131.
(3) Trasatti, S. Electrocatalysis in the Anodic Evolution of Oxygen and Chlorine. *Electrochim. Acta* **1984**, *29*, 1503−1512.
(4) Trasatti, S.; Buzzanca, G. Ruthenium Dioxide: A New Interesting Electrode Material. Solid State Structure and Electrochemical Behaviour. *J. Electroanal. Chem. Interfacial Electrochem.* **1971**, *29*, A1−A5.
(5) Lettenmeier, P.; Majchel, J.; Wang, L.; Saveleva, V. A.; Zafeiratos, S.; Savinova, E. R.; Gallet, J.-J.; Bournel, F.; Gago, A. S.; Friedrich, K. A. Highly Active Nano-Sized Iridium Catalysts: Synthesis and Operando Spectroscopy in a Proton Exchange Membrane Electrolyzer. *Chem. Sci.* **2018**, *9*, 3570−3579.
(6) Seitz, L. C.; Dickens, C. F.; Nishio, K.; Hikita, Y.; Montoya, J.; Doyle, A.; Kirk, C.; Vojvodic, A.; Hwang, H. Y.; Norskov, J. K.; Jaramillo, T. F. A Highly Active and Stable IrOx/SrIrO3 Catalyst for the Oxygen Evolution Reaction. *Science* **2016**, *353*, 1011−1014.
(7) Wang, L.; Song, F.; Ozouf, G.; Geiger, D.; Morawietz, T.; Handl, M.; Gazdzicki, P.; Beauger, C.; Kaiser, U.; Hiesgen, R.; Gago, A. S.; Friedrich, K. A. Improving the Activity and Stability of Ir Catalysts for PEM Electrolyzer Anodes by SnO_2:Sb Aerogel Supports: Does V Addition Play an Active Role in Electrocatalysis? *J. Mater. Chem. A* **2017**, *5*, 3172−3178.
(8) Oh, H. S.; Nong, H. N.; Strasser, P. Preparation of Mesoporous Sb-, F-, and in-Doped SnO2 bulk Powder with High Surface Area for Use as Catalyst Supports in Electrolytic Cells. *Adv. Funct. Mater.* **2015**, *25*, 1074−1081.
(9) Oh, H.-S.; Nong, H. N.; Reier, T.; Bergmann, A.; Gliech, M.; Ferreira de Araújo, J.; Willinger, E.; Schlögl, R.; Teschner, D.; Strasser, P. Electrochemical Catalyst−Support Effects and Their Stabilizing Role for IrO x Nanoparticle Catalysts during the Oxygen Evolution Reaction. *J. Am. Chem. Soc.* **2016**, *138*, 12552−12563.
(10) Nong, H. N.; Oh, H.-S.; Reier, T.; Willinger, E.; Willinger, M.-G.; Petkov, V.; Teschner, D.; Strasser, P. Oxide-Supported IrNiO(x) Core-Shell Particles as Efficient, Cost-Effective, and Stable Catalysts for Electrochemical Water Splitting. *Angew. Chem., Int. Ed.* **2015**, *54*, 2975−2979.
(11) Trasatti, S. Electrocatalysis: Understanding the Success of DSA. *Electrochim. Acta* **2000**, *45*, 2377−2385.
(12) Audichon, T.; Napporn, T. W.; Canaff, C.; Morais, C.; Comminges, C.; Kokoh, K. B. IrO_2 Coated on RuO_2 as Efficient and Stable Electroactive Nanocatalysts for Electrochemical Water Splitting. *J. Phys. Chem. C* **2016**, *120*, 2562−2573.
(13) Lodi, G.; Sivieri, E.; De Battisti, A.; Trasatti, S. Ruthenium Dioxide-Based Film Electrodes. *J. Appl. Electrochem.* **1978**, *8*, 135−143.
(14) Siracusano, S.; Van Dijk, N.; Payne-Johnson, E.; Baglio, V.; Aricò, A. S. Nanosized IrOx and IrRuOx Electrocatalysts for the O2evolution Reaction in PEM Water Electrolysers. *Appl. Catal., B* **2015**, *164*, 488−495.
(15) Siracusano, S.; Baglio, V.; D'Urso, C.; Antonucci, V.; Aricò, A. S. Preparation and Characterization of Titanium Suboxides as Conductive Supports of IrO2 Electrocatalysts for Application in SPE Electrolysers. *Electrochim. Acta* **2009**, *54*, 6292−6299.
(16) Lewinski, K. A.; van der Vliet, D.; Luopa, S. M. NSTF Advances for PEM Electrolysis - the Effect of Alloying on Activity of NSTF Electrolyzer Catalysts and Performance of NSTF Based PEM Electrolyzers. *ECS Trans.* **2015**, *69*, 893−917.
(17) Vesborg, P. C. K.; Jaramillo, T. F. Addressing the Terawatt Challenge: Scalability in the Supply of Chemical Elements for Renewable Energy. *RSC Adv.* **2012**, *2*, 7933−7947.
(18) Castanheira, L.; Dubau, L.; Mermoux, M.; Berthome, G.; Caque, N.; Rossinot, E.; Chatenet, M.; Maillard, F. Carbon Corrosion in Proton-Exchange Membrane Fuel Cells: From Model Experiments to Real-Life Operation in Membrane Electrode Assemblies. *ACS Catal.* **2014**, *4*, 2258−2267.
(19) Castanheira, L.; Silva, W. O.; Lima, F. H. B.; Crisci, A.; Dubau, L.; Maillard, F. Carbon Corrosion in Proton-Exchange Membrane Fuel Cells: Effect of the Carbon Structure, the Degradation Protocol, and the Gas Atmosphere. *ACS Catal.* **2015**, *5*, 2184−2194.
(20) Oh, H. S.; Nong, H. N.; Reier, T.; Bergmann, A.; Gliech, M.; Ferreira De Araújo, J.; Willinger, E.; Schlögl, R.; Teschner, D.; Strasser, P. Electrochemical Catalyst-Support Effects and Their Stabilizing Role for IrOxNanoparticle Catalysts during the Oxygen Evolution Reaction. *J. Am. Chem. Soc.* **2016**, *138*, 12552−12563.
(21) Ledendecker, M.; Geiger, S.; Hengge, K.; Lim, J.; Cherevko, S.; Mingers, A. M.; Göhl, D.; Fortunato, G. V.; Jalalpoor, D.; Schüth, F.; Scheu, C.; Mayrhofer, K. J. J. Towards Maximized Utilization of Iridium for the Acidic Oxygen Evolution Reaction. *Nano Res.* **2019**, *12*, 2275−2280.
(22) Smith, Y. R.; Ray, R. S.; Carlson, K.; Sarma, B.; Misra, M. Self-Ordered Titanium Dioxide Nanotube Arrays: Anodic Synthesis and Their Photo/Electro-Catalytic Applications. *Materials* **2013**, *6*, 2892−2957.
(23) DeWitt, S.; Thornton, K. Anodic Oxide Nanostructures and Their Applications in Energy Generation and Storage. *Nanomaterials for Sustainable Energy*; ACS Symposium Series; ACS Publications: 2015; 19−39.
(24) Roy, P.; Berger, S.; Schmuki, P. TiO_2 Nanotubes: Synthesis and Applications. *Angew. Chem., Int. Ed.* **2011**, *50*, 2904−2939.
(25) Nowotny, M. K.; Bak, T.; Nowotny, J. Electrical Properties and Defect Chemistry of TiO_2 Single Crystal. I. Electrical Conductivity. *J. Phys. Chem. B* **2006**, *110*, 16270−16282.
(26) Padture, N. P.; Wei, X. Hydrothermal Synthesis of Thin Films of Barium Titanate Ceramic Nano-Tubes at 200 °C. *J. Am. Ceram. Soc.* **2003**, *86*, 2215−2217.
(27) Zhang, J.; Bang, J. H.; Tang, C.; Kamat, P. V. Tailored TiO_2−$SrTiO_3$ Heterostructure Nanotube Arrays for Improved Photoelectrochemical Performance. *ACS Nano* **2010**, *4*, 387−395.

(28) Soderznik, K. Z.; Fabrega, C.; Hernandez-Ramirez, F.; Prades, J. D.; Čeh, M. $BaTiO_3$ Based Nanostructures for Humidity Sensing Applications. *Proceedings* **2019**, *15*, No. 9.
(29) Chisaka, M. Creation of Oxygen Reduction Reaction Active Sites on Titanium Oxynitride without Increasing the Nitrogen Doping Level. *Phys. Chem. Chem. Phys.* **2018**, *20*, 15613−15617.
(30) Suhadolnik, L.; Lašič Jurković, D.; Likozar, B.; Bele, M.; Drev, S.; Čeh, M. Structured Titanium Oxynitride (TiO_xN_y) Nanotube Arrays for a Continuous Electrocatalytic Phenol-Degradation Process: Synthesis, Characterization, Mechanisms and the Chemical Reaction Micro-Kinetics. *Appl. Catal., B* **2019**, *257*, No. 117894.
(31) Loncar, A.; Moriau, L.; Stojanovski, K.; Ruiz-Zepeda, F.; Jovanovic, P.; Bele, M.; Gaberscek, M.; Hodnik, N. $Ir/TiON_x/C$ High-Performance Oxygen Evolution Reaction Nanocomposite Electrocatalysts in Acidic Media: Synthesis, Characterization and Electrochemical Benchmarking Protocol. *J. Phys. Energy* **2020**, *2*, No. 02LT01.
(32) Zorko, M.; Jozinović, B.; Bele, M.; Hodnik, N.; Gaberšček, M. SEM Method for Direct Visual Tracking of Nanoscale Morphological Changes of Platinum Based Electrocatalysts on Fixed Locations upon Electrochemical or Thermal Treatments. *Ultramicroscopy* **2014**, *140*, 44−50.
(33) Hodnik, N.; Cherevko, S. Spot the Difference at the Nanoscale: Identical Location Electron Microscopy in Electrocatalysis. *Curr. Opin. Electrochem.* **2019**, *15*, 73−82.
(34) Hodnik, N.; Zorko, M.; Bele, M.; Hočevar, S.; Gaberšček, M. Identical Location Scanning Electron Microscopy: A Case Study of Electrochemical Degradation of PtNi Nanoparticles Using a New Nondestructive Method. *J. Phys. Chem. C* **2012**, *116*, 21326−21333.
(35) Kabekkodu, S. *PDF-4+*; ICCD, International Centre for Diffraction Data: Newton Square, PA, 2016.
(36) Alia, S. M.; Rasimick, B.; Ngo, C.; Neyerlin, K. C.; Kocha, S. S.; Pylypenko, S.; Xu, H.; Pivovar, B. S. Activity and Durability of Iridium Nanoparticles in the Oxygen Evolution Reaction. *J. Electrochem. Soc.* **2016**, *163*, F3105−F3112.
(37) El-Sayed, H. A.; Weiß, A.; Olbrich, L. F.; Putro, G. P.; Gasteiger, H. A. OER Catalyst Stability Investigation Using RDE Technique: A Stability Measure or an Artifact? *J. Electrochem. Soc.* **2019**, *166*, F458−F464.
(38) Giannozzi, P.; Andreussi, O.; Brumme, T.; Bunau, O.; Buongiorno Nardelli, M.; Calandra, M.; Car, R.; Cavazzoni, C.; Ceresoli, D.; Cococcioni, M.; Colonna, N.; Carnimeo, I.; Dal Corso, A.; de Gironcoli, S.; Delugas, P.; DiStasio, R. A.; Ferretti, A.; Floris, A.; Fratesi, G.; Fugallo, G.; Gebauer, R.; Gerstmann, U.; Giustino, F.; Gorni, T.; Jia, J.; Kawamura, M.; Ko, H.-Y.; Kokalj, A.; Küçükbenli, E.; Lazzeri, M.; Marsili, M.; Marzari, N.; Mauri, F.; Nguyen, N. L.; Nguyen, H.-V.; Otero-de-la-Roza, A.; Paulatto, L.; Poncé, S.; Rocca, D.; Sabatini, R.; Santra, B.; Schlipf, M.; Seitsonen, A. P.; Smogunov, A.; Timrov, I.; Thonhauser, T.; Umari, P.; Vast, N.; Wu, X.; Baroni, S. Advanced Capabilities for Materials Modelling with Quantum ESPRESSO. *J. Phys.: Condens. Matter* **2017**, *29*, No. 465901.
(39) Anisimov, V. I.; Zaanen, J.; Andersen, O. K. Band Theory and Mott Insulators: Hubbard U Instead of Stoner I. *Phys. Rev. B* **1991**, *44*, 943−954.
(40) Cococcioni, M.; De Gironcoli, S. Linear Response Approach to the Calculation of the Effective Interaction Parameters in the LDA + U Method. *Phys. Rev. B: Condens. Matter Mater. Phys.* **2005**, *71*, No. 035105.
(41) Perdew, J. P.; Burke, K.; Ernzerhof, M. Generalized Gradient Approximation Made Simple. *Phys. Rev. Lett.* **1996**, *77*, 3865−3868.
(42) Dal Corso, A. Pseudopotentials Periodic Table: From H to Pu. *Comput. Mater. Sci.* **2014**, *95*, 337−350.
(43) pslibrary. https://dalcorso.github.io/pslibrary/.
(44) Timrov, I.; Marzari, N.; Cococcioni, M. Hubbard Parameters from Density-Functional Perturbation Theory. *Phys. Rev. B* **2018**, *98*, No. 085127.
(45) Methfessel, M.; Paxton, A. T. High-Precision Sampling for Brillouin-Zone Integration in Metals. *Phys. Rev. B* **1989**, *40*, 3616−3621.
(46) Sluban, M.; Umek, P.; Jagličić, Z.; Buh, J.; Šmitek, P.; Mrzel, A.; Bittencourt, C.; Guttmann, P.; Delville, M.-H.; Mihailović, D.; Arčon, D. Controlling Disorder and Superconductivity in Titanium Oxynitride Nanoribbons with Anion Exchange. *ACS Nano* **2015**, *9*, 10133−10141.
(47) Ehteshami, S. M. M.; Taheri, A.; Chan, S. H. A Review on Ions Induced Contamination of Polymer Electrolyte Membrane Fuel Cells, Poisoning Mechanisms and Mitigation Approaches. *J. Ind. Eng. Chem.* **2016**, *34*, 1−8.
(48) Sarraf, M.; Razak, A.; Crum, R.; Gámez, C.; Ramirez, B.; Kasim, N.; Nasiri-Tabrizi, B.; Gupta, V.; Sukiman, N.; Basirun, W. Adhesion Measurement of Highly-Ordered TiO2 Nanotubes on Ti-6Al-4 V Alloy. *Process. Appl. Ceram.* **2017**, *11*, 311−321.
(49) Pfeifer, V.; Jones, T. E.; Velasco Vélez, J. J.; Massué, C.; Arrigo, R.; Teschner, D.; Girgsdies, F.; Scherzer, M.; Greiner, M. T.; Allan, J.; Hashagen, M.; Weinberg, G.; Piccinin, S.; Hävecker, M.; Knop-Gericke, A.; Schlögl, R. The Electronic Structure of Iridium and Its Oxides. *Surf. Interface Anal.* **2016**, *48*, 261−273.
(50) Han, J. H.; Bang, J. H. A Hollow Titanium Oxynitride Nanorod Array as an Electrode Substrate Prepared by the Hot Ammonia-Induced Kirkendall Effect. *J. Mater. Chem. A* **2014**, *2*, 10568−10576.
(51) Alia, S. M.; Hurst, K. E.; Kocha, S. S.; Pivovar, B. S. Mercury Underpotential Deposition to Determine Iridium and Iridium Oxide Electrochemical Surface Areas. *J. Electrochem. Soc.* **2016**, *163*, F3051−F3056.
(52) Kounaves, S. P.; Buffle, J. Deposition and Stripping Properties of Mercury on Iridium Electrodes. *J. Electrochem. Soc.* **1986**, *133*, 2495−2498.
(53) Savinell, R. F.; Zeller, R. L.; Adams, J. A. Electrochemically Active Surface Area: Voltammetric Charge Correlations for Ruthenium and Iridium Dioxide Electrodes. *J. Electrochem. Soc.* **1990**, *137*, 489−494.
(54) Zhao, S.; Yu, H.; Maric, R.; Danilovic, N.; Capuano, C. B.; Ayers, K. E.; Mustain, W. E. Calculating the Electrochemically Active Surface Area of Iridium Oxide in Operating Proton Exchange Membrane Electrolyzers. *J. Electrochem. Soc.* **2015**, *162*, F1292−F1298.
(55) McCrory, C. C. L.; Jung, S.; Peters, J. C.; Jaramillo, T. F. Benchmarking Heterogeneous Electrocatalysts for the Oxygen Evolution Reaction. *J. Am. Chem. Soc.* **2013**, *135*, 16977−16987.
(56) Bizzotto, F.; Quinson, J.; Zana, A.; Kirkensgaard, J. J. K.; Dworzak, A.; Oezaslan, M.; Arenz, M. Ir Nanoparticles with Ultrahigh Dispersion as Oxygen Evolution Reaction (OER) Catalyst: Synthesis and Activity Benchmarking. *Catal. Sci. Technol.* **2019**, *9*, 6345−6356.
(57) Watzele, S.; Hauenstein, P.; Liang, Y.; Xue, S.; Fichtner, J.; Garlyyev, B.; Scieszka, D.; Claudel, F.; Maillard, F.; Bandarenka, A. S. Determination of Electroactive Surface Area of Ni-, Co-, Fe-, and Ir-Based Oxide Electrocatalysts. *ACS Catal.* **2019**, *9*, 9222−9230.
(58) Kim, W.-R.; Park, H.; Choi, W.-Y. Conical Islands of TiO_2 Nanotube Arrays in the Photoelectrode of Dye-Sensitized Solar Cells. *Nanoscale Res. Lett.* **2015**, *10*, No. 63.
(59) Bele, M.; Stojanovski, K.; Jovanovič, P.; Moriau, L.; Koderman Podboršek, G.; Moškon, J.; Umek, P.; Sluban, M.; Dražič, G.; Hodnik, N.; Gaberšček, M. Towards Stable and Conductive Titanium Oxynitride High-Surface-Area Support for Iridium Nanoparticles as Oxygen Evolution Reaction Electrocatalyst. *ChemCatChem* **2019**, *11*, 5038−5044.
(60) Chen, P.; Khetan, A.; Yang, F.; Migunov, V.; Weide, P.; Stürmer, S. P.; Guo, P.; Kähler, K.; Xia, W.; Mayer, J.; Pitsch, H.; Ulrich, S.; Muhler, M. Experimental and Theoretical Understanding of Nitrogen-Doping-Induced Strong Metal−Support Interactions in Pd/TiO_2 Catalysts for Nitrobenzene Hydrogenation. *ACS Catal.* **2017**, *7*, 1197−1206.
(61) Foger, K.; Anderson, J. R. Thermally Stable SMSI Supports: Iridium Supported on TiO_2-Al2O3 and on Ce-Stabilized Anatase. *Appl. Catal.* **1986**, *23*, 139−155.
(62) Chen, G.; Bare, S. R.; Mallouk, T. E. Development of Supported Bifunctional Electrocatalysts for Unitized Regenerative Fuel Cells. *J. Electrochem. Soc.* **2002**, *149*, No. A1092.

(63) Reier, T.; Teschner, D.; Lunkenbein, T.; Bergmann, a.; Selve, S.; Kraehnert, R.; Schlogl, R.; Strasser, P. Electrocatalytic Oxygen Evolution on Iridium Oxide: Uncovering Catalyst-Substrate Interactions and Active Iridium Oxide Species. *J. Electrochem. Soc.* **2014**, *161*, F876−F882.
(64) Scheuermann, A. G.; Prange, J. D.; Gunji, M.; Chidsey, C. E. D.; McIntyre, P. C. Effects of Catalyst Material and Atomic Layer Deposited TiO_2 Oxide Thickness on the Water Oxidation Performance of Metal-Insulator-Silicon Anodes. *Energy Environ. Sci.* **2013**, *6*, 2487−2496.
(65) Cherevko, S.; Geiger, S.; Kasian, O.; Mingers, A.; Mayrhofer, K. J. J. Oxygen Evolution Activity and Stability of Iridium in Acidic Media. Part 1. − Metallic Iridium. *J. Electroanal. Chem.* **2016**, *773*, 69−78.
(66) Cherevko, S.; Geiger, S.; Kasian, O.; Mingers, A.; Mayrhofer, K. J. J. Oxygen Evolution Activity and Stability of Iridium in Acidic Media. Part 2. − Electrochemically Grown Hydrous Iridium Oxide. *J. Electroanal. Chem.* **2016**, *774*, 102−110.
(67) Kasian, O.; Grote, J.; Geiger, S.; Cherevko, S.; Mayrhofer, K. J. J. The Common Intermediates of Oxygen Evolution and Dissolution Reactions during Water Electrolysis on Iridium. *Angew. Chem., Int. Ed.* **2018**, *57*, 2488−2491.
(68) Zeradjanin, A. R.; La Mantia, F.; Masa, J.; Schuhmann, W. Utilization of the Catalyst Layer of Dimensionally Stable Anodes—Interplay of Morphology and Active Surface Area. *Electrochim. Acta* **2012**, *82*, 408−414.
(69) Zeradjanin, A. R.; Topalov, A. A.; Van Overmeere, Q.; Cherevko, S.; Chen, X.; Ventosa, E.; Schuhmann, W.; Mayrhofer, K. J. J. Rational Design of the Electrode Morphology for Oxygen Evolution-Enhancing the Performance for Catalytic Water Oxidation. *RSC Adv.* **2014**, *4*, 9579−9587.
(70) Trieu, V.; Schley, B.; Natter, H.; Kintrup, J.; Bulan, A.; Hempelmann, R. RuO_2-Based Anodes with Tailored Surface Morphology for Improved Chlorine Electro-Activity. *Electrochim. Acta* **2012**, *78*, 188−194.
(71) Zeradjanin, A. R.; Ventosa, E.; Bondarenko, A. S.; Schuhmann, W. Evaluation of the Catalytic Performance of Gas-Evolving Electrodes Using Local Electrochemical Noise Measurements. *ChemSusChem* **2012**, *5*, 1905−1911.
(72) Chen, X.; Maljusch, A.; Rincón, R. A.; Battistel, A.; Bandarenka, A. S.; Schuhmann, W. Local Visualization of Catalytic Activity at Gas Evolving Electrodes Using Frequency-Dependent Scanning Electrochemical Microscopy. *Chem. Commun.* **2014**, *50*, 13250−13253.
(73) Ohno, H.; Nohara, S.; Kakinuma, K.; Uchida, M.; Miyake, A.; Deki, S.; Uchida, H. Remarkable Mass Activities for the Oxygen Evolution Reaction at Iridium Oxide Nanocatalysts Dispersed on Tin Oxides for Polymer Electrolyte Membrane Water Electrolysis. *J. Electrochem. Soc.* **2017**, *164*, F944−F947.
(74) Alia, S. M.; Shulda, S.; Ngo, C.; Pylypenko, S.; Pivovar, B. S. Iridium-Based Nanowires as Highly Active, Oxygen Evolution Reaction Electrocatalysts. *ACS Catal.* **2018**, *8*, 2111−2120.
(75) Godínez-Salomón, F.; Albiter, L.; Alia, S. M.; Pivovar, B. S.; Camacho-Forero, L. E.; Balbuena, P. B.; Mendoza-Cruz, R.; Arellano-Jimenez, M. J.; Rhodes, C. P. Self-Supported Hydrous Iridium-Nickel Oxide Two-Dimensional Nanoframes for High Activity Oxygen Evolution Electrocatalysts. *ACS Catal.* **2018**, *8*, 10498−10520.
(76) Jensen, A. W.; Sievers, G. W.; Jensen, K. D.; Quinson, J.; Arminio-Ravelo, J. A.; Brüser, V.; Arenz, M.; Escudero-Escribano, M. Self-Supported Nanostructured Iridium-Based Networks as Highly Active Electrocatalysts for Oxygen Evolution in Acidic Media. *J. Mater. Chem. A* **2020**, *8*, 1066−1071.
(77) Seo, S. G.; Park, C. H.; Kim, H. Y.; Nam, W. H.; Jeong, M.; Choi, Y. N.; Lim, Y. S.; Seo, W. S.; Kim, S. J.; Lee, J. Y.; Cho, Y. S. Preparation and Visible-Light Photocatalysis of Hollow Rock-Salt TiO 1-XNx Nanoparticles. *J. Mater. Chem. A* **2013**, *1*, 3639−3644.

https://dx.doi.org/10.1021/acscatal.0c03688
ACS Catal. 2020, 10, 13688−13700